Field-domain rapid-scan EPR at 240 GHz for studies of protein functional dynamics at room temperature

Brad D. Price [a,b,*], Antonín Sojka [a,b], Shiny Maity [c,d], I. Marcelo Chavez [c], Matthieu Starck [e], Maxwell Z. Wilson [f], Songi Han [c,d], Mark S. Sherwin [a,b]

[a] Department of Physics, University of California, Santa Barbara, 93106, CA, USA
[b] Institute for Terahertz Science and Technology, University of California, Santa Barbara, 93106, CA, USA
[c] Department of Chemistry, University of California, Santa Barbara, 93106, CA, USA
[d] Department of Chemistry, Northwestern University, 633 Clark Street, Evanston, 60208, IL, USA
[e] Department of Chemistry, Durham University, Durham, DH13LE, UK
[f] Department Molecular, Cellular, and Developmental Biology, University of California, Santa Barbara, 93106, CA, USA

ARTICLE INFO

ABSTRACT

We present field-domain rapid-scan (RS) electron paramagnetic resonance (EPR) at 8.6 T and 240 GHz. To enable this technique, we upgraded a home-built EPR spectrometer with an FPGA-enabled digitizer and real-time processing software. The software leverages the Hilbert transform to recover the in-phase (I) and quadrature (Q) channels, and therefore the raw absorptive and dispersive signals, χ' and χ'', from their combined magnitude ($\sqrt{I^2 + Q^2}$). Averaging a magnitude is simpler than real-time coherent averaging and has the added benefit of permitting long-timescale signal averaging (up to at least 2.5×10^6 scans) because it eliminates the effects of source-receiver phase drift. Our rapid-scan (RS) EPR provides a signal-to-noise ratio that is approximately twice that of continuous wave (CW) EPR under the same experimental conditions, after scaling by the square root of acquisition time. We apply our RS EPR as an extension of the recently reported time-resolved Gd-Gd EPR (TiGGER) [Maity et al., 2023], which is able to monitor inter-residue distance changes during the photocycle of a photoresponsive protein through changes in the Gd-Gd dipolar couplings. RS, opposed to CW, returns field-swept spectra as a function of time with 10 ms time resolution, and thus, adds a second dimension to the static field transients recorded by TiGGER. We were able to use RS TiGGER to track time-dependent and temperature-dependent kinetics of AsLOV2, a light-activated phototropin domain found in oats. The results presented here combine the benefits of RS EPR with the improved spectral resolution and sensitivity of Gd chelates at high magnetic fields. In the future, field-domain RS EPR at high magnetic fields may enable studies of other real-time kinetic processes with time resolutions that are otherwise difficult to access in the solution state.

1. Introduction

Rapid-scan (RS) electron paramagnetic resonance (EPR) is a technique that has received increased attention in recent decades [1–11]. It can provide substantial benefits compared to conventional CW EPR, with improved signal-to-noise (SNR) ratio for equivalent acquisition times as well as the ability to record entire field-swept spectra with high temporal resolution [12–17]. In RS EPR, either the source frequency or the applied magnetic field is rapidly swept to record a spectrum. Frequency sweeps can be done extremely quickly using an arbitrary waveform generator (AWG) or voltage-controlled oscillator (up to 10^7 T/s [18,19]) and do not generate eddy currents in metallic

elements. In contrast, field sweeps are much slower (10^3 T/s) and do generate eddy currents [20], but do not suffer from frequency-dependent standing wave modes in the quasioptics, as the source frequency is fixed [21]. It is also comparatively cost-effective and simpler to implement field-domain rapid-scanning in a fixed-frequency CW EPR spectrometer because a variable-frequency source and detector are not required.

To date, RS EPR has been primarily utilized at low field (*i.e.* "X-band", 9.6 GHz and 342 mT), where commercial options exist. However, there are benefits to performing EPR at high magnetic fields and frequencies (>3.6 T and >100 GHz): larger fields improve spectral

---

resolution, increase sensitivity through increased electron spin polarization, and can even *decrease* the width of an EPR line in the case of $-1/2 \to 1/2$ transitions of paramagnetic species with non-integer spin $>1/2$, if the primary broadening mechanism is zero-field splitting. In particular, as reported in [22–24] the linewidth of the $-1/2 \to 1/2$ transition in Gd-sTPATCN, a highly-symmetric gadolinium spin label with spin 7/2, has been shown to decrease to less than 10 Gauss at 8.6 T (240 GHz) in sufficiently dilute samples, due to its small zero-field splitting and otherwise symmetric, isotropic EPR spectrum. Hence, dipolar broadening of Gd spin labels at 8.6 T is visible if other Gd spins are sufficiently close (< 4 nm separation), making their linewidth useful for probing distances between residues in spin-labeled proteins [22].

Combining the benefits of high-field and rapid-scan EPR is still rare [11,18,25], but has been demonstrated up to 330 GHz [26]. The first demonstration of rapid-scan at high field was in the frequency domain [18]. Resonator-free, high-field spectrometers — such as the one used in this study — do not limit the range of frequencies that may be used [20], and thus can provide access to broad spectra when the frequency is swept. Still, frequency-domain rapid scanning is complicated to implement given the instability caused by standing waves.

Implementing field-domain modulation is less complicated than frequency-domain, but many EPR resonance lines are too broad for a ~100 G field-domain modulation coil to achieve meaningful results. However, the $-1/2 \to 1/2$ transition in Gd-sTPATCN is sufficiently narrow to sweep through with a ~100 G modulation coil, thereby enabling field-domain RS EPR of protein samples of interest at high magnetic field; to our knowledge, this report is the first demonstration of field-domain RS EPR above X-band.

For this experiment, a function generator and modulation coil are required in order to sweep through an entire EPR transition of interest in a matter of microseconds. This implementation also requires a digitizer with a sampling rate of order 500 MSa/s (see below) and real-time onboard averaging that can continuously average rapid scans as they are acquired (thousands of points, updating at tens of kHz), in order to operate at an achievable data throughput and minimize post-processing. To enable field-domain rapid-scan in the homebuilt EPR spectrometer housed at UCSB's Institute for Terahertz Science and Technology (ITST), hardware and software upgrades were required. One such upgrade was the implementation of the recently reported quasioptical sample holder that greatly improves SNR by reducing the intensity of baseline relative to signal [17]. The sample holder also makes it possible to finely position the sample at a B_1 maximum to amplify the resulting EPR response. It does not contain metallic components within the coil and all metallic components are quite far from the coil center, eliminating the background effects of eddy currents in rapid-scan experiments: the nearest metallic element is a copper waveguide that is approximately 1.25 mm from the top of the coil along its field axis (7.25 mm from the center of the coil) and the cylindrical cryostat that houses the probe is 6 cm in diameter, which is quite far away from the 2.5 cm outer diameter of the coil (and 3 cm from its center) [17]. The second upgrade was the installation and programming of a field-programmable gate array (FPGA)-enabled digitizer for rapid data acquisition and real-time averaging. In total, the work presented here represents a large leap in field-domain RS EPR from 9.4 GHz to 240 GHz.

We have recently shown that high-field RS EPR can be used to track solid-state kinetic processes [17]. In the current study, we demonstrate the potential of this new approach to directly measure time-resolved inter-residue distances after inducing conformational changes of a protein in solution, addressing an important frontier in biology. For this demonstration, we have chosen the blue-light activated phototropin domain AsLOV2, which is an important protein for regulating photosynthesis in plants [27,28], and is of interest to the optogenetic community [29–33].

2. Experimental design

All experiments were done using the homebuilt EPR spectrometer at ITST. The spectrometer operates in field domain with a 12.5 T field-swept magnet (Oxford Instruments, Inc., UK), 240 GHz source (~30 mW output power, Virginia Diodes, Inc., USA), and Schottky-diode based subharmonically-mixed heterodyne receiver (WR4.3SHM with single-sideband noise temperature approx. 1400 K and 8 dB conversion loss, Virginia Diodes, Inc., USA) that returns the EPR signal at an intermediate frequency (IF) of 10 GHz. All rapid-scan experiments presented here made use of the quasioptical sample holder presented in Sojka et al. [17] to maximize the signal-to-noise ratio, which in turn enhances the temporal resolution of kinetic processes of interest. Specific IF stage components are listed in S.I. sec. S1 and additional spectrometer details that do not pertain specifically to rapid-scan operation can be found elsewhere (*e.g.*, [34,35]).

Field-domain RS EPR is achieved by driving a modulation coil with a sinusoidal AC current (~100 mA RMS; produced by 8111 A function generator, Hewlett-Packard, USA) to sweep rapidly through the resonance (modulation field is ~100 G peak-to-peak at ~25 kHz, depending on the inductance and number of turns of the individual coil, as well as the capacitance of in-series capacitor, which we usually set to 10 nF). Therefore the peak sweep rate, at the center of a sinusoidal sweep, is approximately 600 T/s. The modulation coil strength at a given frequency may be improved by reducing the AC impedance of the coil of choice or amplifying the driver current. This can be done with Litz wire [36] or an amplifier circuit like those reported in refs. [37–39]. Because this coil is approximately 5× smaller in each dimension than coils used for X-band RS EPR, it can be driven to similar field strengths with much lower currents. This reduces spurious microphonic effects as well as associated eddy current effects and parasitic signals to negligible levels [40]. The function generator that drives the modulation coil is also used to trigger data acquisition at the digitizer (16-bit PXIe-5673, National Instruments™, USA) so that field sweeps start and stop at repeatable field positions. Only the low-to-high field sweeps are recorded so that the digitizer has time to arm and trigger before each low-to-high sweep.

After detection and subharmonic mixing, the IF signal that contains the EPR spectrum is variably attenuated to control input power, amplified, then IQ-mixed with an in-phase and quadrature 10.10 GHz local oscillator (LO) signal (MLSL-0911, Micro Lambda Wireless, Inc., USA) that is phase-locked to the subharmonic mixer LO. This mixing results in a 100 MHz carrier frequency (see IF stage block diagram in Fig. 1) that is directly digitized and subsequently added in quadrature by a field-programmable gate array (Xilinx KU040 FPGA, Advanced Micro Devices, Inc., USA) onboard an AC-coupled 500 MS/s, 225 MHz input bandwidth digitizer.

Because we detect a significant amount of co-polar leakage, (*i.e.*, reflected source power parallel to the input polarization that is not a result of induction mode EPR absorption), the signals that are digitized contain a large DC offset. Somewhat surprisingly, due to this offset, we are able to extract both the dispersion, χ', and absorption, χ'', by only recording the magnitude of the input IF signal ($\sqrt{I^2 + Q^2}$). To demonstrate, assume one channel contains χ' and some DC offset, a, and the other contains χ'' and some DC offset, b, we can write the magnitude of the digitized signal, S, up to a scaling factor, as:

$$|S| \propto \sqrt{I^2 + Q^2} = \sqrt{(\chi' + a)^2 + (\chi'' + b)^2}. \tag{1}$$

Then, since the co-polar leakage is large compared to the EPR signal, the DC offset in each channel is large compared to the susceptibility ($a \gg \chi'$ and $b \gg \chi''$). Applying the binomial approximation twice returns:

$$|S| \underset{\sim}{\propto} \sqrt{a^2 + b^2} + \frac{a\chi' + b\chi''}{\sqrt{a^2 + b^2}}. \tag{2}$$
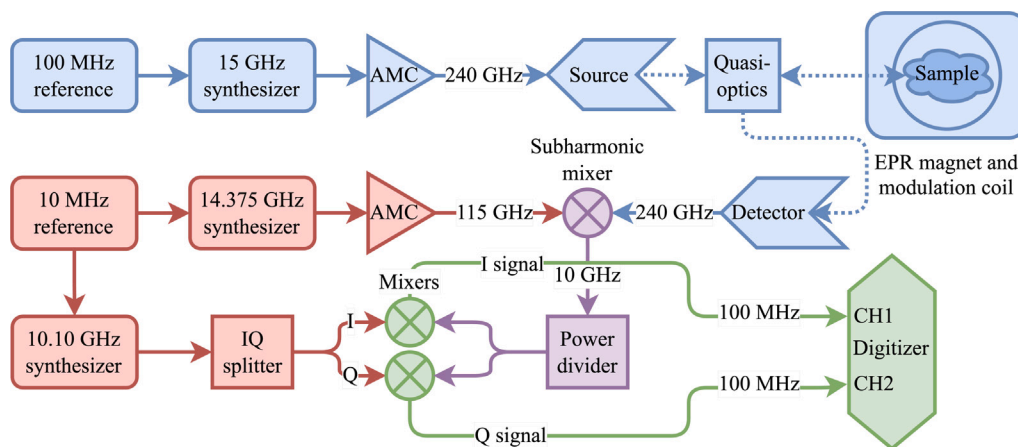
Fig. 1. Simplified block diagram of the rapid-scan EPR spectrometer. Signal acquired by the digitizer is sampled every 2 ns and time and field-domain traces are summed at the modulation frequency of ~25 kHz. An amplifier-multiplier chain (AMC) that appears in the source chain (blue, top) multiplies the 15 GHz LO frequency 16×. The source power emitted is ~30 mW at 240 GHz. An AMC in the detector chain (red, middle) multiplies the 14.375 GHz LO frequency 8×. The resulting 240 GHz and 115 GHz signals are subharmonically mixed (WR4.3SHM, Virginia Diodes, Inc., USA) to 10 GHz for amplification, filtering, and further mixing with 0° and 90° 10.10 GHz reference signals, which produces two orthogonal signals at a 100 MHz carrier frequency. The 100 MHz modulated signals (green, bottom right) are then digitized by an FPGA-enabled digitizer. The 100 MHz and 10 MHz reference sources do not need to be phase-locked because of the phase-insensitive magnitude averaging technique used. Solid lines represent SMA cables carrying electronic signals and the dotted lines represent electromagnetic waves that propagate through quasioptical components and in-and-out of the EPR magnet where the sample is located. RF amplifiers and variable attenuators are omitted here for simplicity. Individual part numbers for the components shown here, as well as those that are omitted, are provided in S.I. sec. S1.

Then, subtracting the Hilbert transform, $\mathcal{H}$, of $|S|$ provides us with an analytic signal (which we denote $\widetilde{|S|}$) that can be deconvolved using the algorithm in Tseytlin [41].

$$\widetilde{|S|} = |S| - i\mathcal{H}\{|S|\} \underset{\sim}{\propto} \sqrt{a^2 + b^2} + \frac{a\chi' + b\chi''}{\sqrt{a^2 + b^2}} - i\left(\frac{-a\chi'' + b\chi'}{\sqrt{a^2 + b^2}}\right). \quad (3)$$

Simplifying and applying a overall phase correction of $\phi = \pi/2 - \tan^{-1}(a/b)$ leaves us with:

$$\widetilde{|S|}e^{i\phi} \underset{\sim}{\propto} (a + ib) + \chi' + i\chi'' \propto S, \quad (4)$$

which is the original signal, S, up to a scaling factor, that contains separable components of both χ' and χ'', our rapid-scan signals of interest. For a full derivation, please see S.I. sec. S2.1.

It is possible to obtain χ' and χ'' by phasing each I and Q signal separately before averaging. In this case, the 100 MHz carrier frequency must remain very stable throughout the experiment so that each sine wave may be precisely aligned. The final result of separately phasing each I and Q signal is the same as the one described above, but implementing the necessary frequency stability is challenging and real-time phasing is much slower computationally; therefore, we instead chose to continuously average magnitudes to maximize the FPGA's ability to perform computations in real time. Importantly, averaging magnitudes eliminates any dependence on phase drift between the source and receiver and thereby enables phase-independent signal averaging. For this reason, the 100 MHz and 10 MHz reference sources shown in Fig. 1 are not required to be phase-locked to one another, and we are not sensitive to phase drifts due to changing temperature, for example.

The magnitude signals are continuously summed a user-specified number of times in the FPGA and transferred to the control PC for further processing (see block diagram in Fig. 2). The control PC computes the root-mean-square time-dependent signal, digitally filters high frequency noise (LabVIEW 21.0 Butterworth low-pass filter with $f_{cutoff} = 25$ MHz), and writes the signal to an experiment file. Currently, the averaging is limited to ≥250 scans (~10 ms with 25 kHz field modulation) due to limitations with memory onboard the digitizer and data throughput rates to the control PC.

Experiment files are processed using Python3 [42]: beginning with Eq. (5), the Hilbert transform is computed from the raw magnitude of I and Q, $r(t) = \sqrt{I^2 + Q^2}$, to return the complex analytic signal of the acquired component,

$$\widetilde{r_a}(t) = r(t) - i * \mathbf{Im}\{\mathbf{H}\{r(t)\}\}, \quad (5)$$

where **H** is scipy.signal.hilbert [43]. As discussed above, this process returns a complex signal that contains both $\chi'(t)$ and $\chi''(t)$ with some DC offset and an unknown phase. Next, a GUI (onefileRapidscan-GUI.py, [42]) is used to implement the deconvolution algorithm for sinusoidal scans developed by Tseytlin [41]. The combination of these programs returns $\chi*$, the complex magnetic susceptibility χ with some phase shift. To obtain the field-swept absorptive and dispersive lineshapes, the spectra must be phased. There are multiple ways to apply the phasing, but a typical method requires minimizing (nulling) any negative values in χ'', the absorptive signal of interest. Symbolically,

$$\chi^*(B) = \mathbf{D}\left\{\widetilde{r_a}(t)\right\}$$
$$e^{i\phi}(\chi' + i\chi'') = \mathbf{D}\left\{\widetilde{r_a}\right\}, \text{ where } \chi^* = e^{i\phi}\chi = e^{i\phi}(\chi' + i\chi'')$$
$$\chi'' = \mathbf{Im}\left\{e^{-i\phi}\mathbf{D}\left\{\widetilde{r_a}\right\}\right\}, \quad (6)$$

where $\chi^*(B)$ is the complex magnetic susceptibility χ as a function of field, B, with unknown phase ϕ; **D** is the deconvolution algorithm from Tseytlin [41]; and χ' and χ'' are the slow-scan dispersive and absorptive signals, respectively.

3. Results

In this study, we apply high-field field-domain RS EPR to study the time-resolved kinetics of Gd(III)-labeled AsLOV2, a phototropin domain that is known to unfold upon blue-light activation [44]. AsLOV2 was spin-labeled at a pair of sites (406 and 537) with Gd-sTPATCN. In its dark state, the EPR spectrum of Gd-labeled AsLOV2 is broadened through dipolar coupling [45]. When illuminated with blue light, the protein is activated to its lit state and the distance between the two spin labels increases, thereby reducing the strength of the dipolar coupling. Previous time-resolved Gd-Gd EPR (TiGGER) measurements on identically-labeled AsLOV2 samples, performed at a fixed magnetic field, confirmed this effect [46].

However, in order to extract quantitative, time-resolved changes in distance under functional conditions, it is necessary to record the entire EPR lineshape of interest at every time step in solution state, which requires RS TiGGER. In this paper, we report time-dependent measurement of EPR lineshapes by RS TiGGER before, during, and after light activation. From these lineshapes, we extract an activation energy of 15.5 ± 1.5 kcal/mol for AsLOV2 refolding using a temperature-dependent Arrhenius plot of refolding rates that agrees well with the NMR-determined values presented in Harper et al. [47].
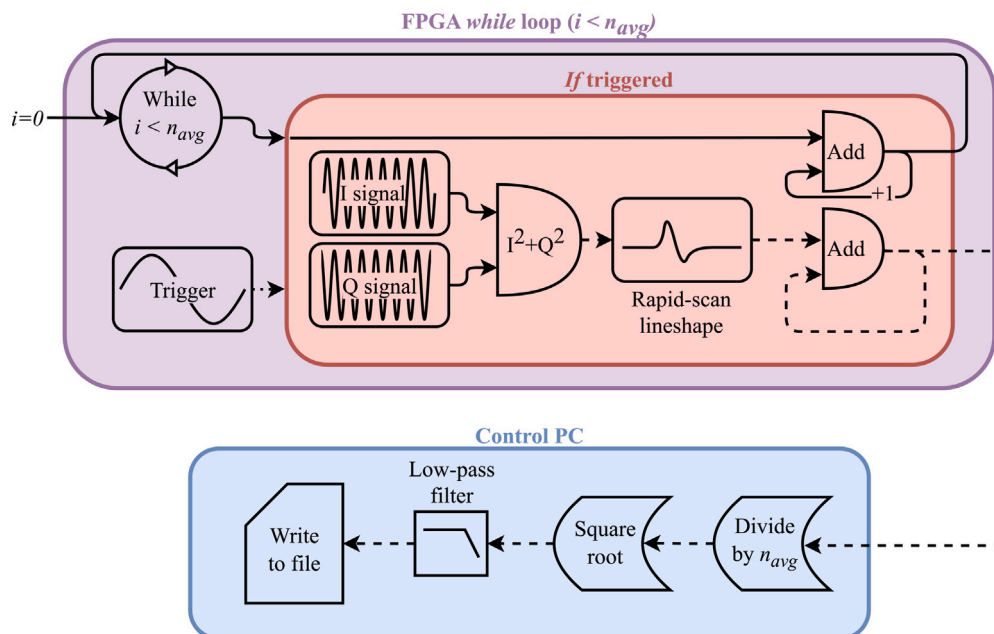
Fig. 2. Digital signal processing block diagram. The AC current that drives the rapid-scan field serves as a data acquisition trigger (~25 kHz), which is looping inside a *while* loop (purple). The trigger activates an acquisition cycle in an *if* loop (red) that proceeds until it executes a user-specified number of times. Inside the *if* loop, the *I* and *Q* signals (100 MHz carrier frequency) are added in quadrature, and then continuously averaged by summing. After the *while* loop has run *n* times, the loop exits, the data is sent to a control PC for additional processing (blue), and the *while* loop is restarted. On the control PC, the root-mean-square signal is calculated and then low-pass filtered at 25 MHz, which removes high frequency noise and harmonics of the carrier frequency while preserving any features that may appear in the rapid-scan spectrum. The data is then written to a file.

3.1. Gd-sTPATCN

Field-domain RS EPR relies on the ability to sweep the entire resonance using the modulation coil, without sweeping the main field. Our modulation coils typically reach field strengths of ~100 G peak-to-peak, and thus, can only be used for RS on lines narrower than 25 G because the Hilbert transform in post-processing requires that the scan extends far past the wings of the resonance. At 8.6 T, Gd-sTPATCN has a full-width at half-maximum linewidth of less than 10 G, even when attached to a protein [23,46], due to its very small zero-field splitting (ZFS) and significant ZFS strain (at 10 K, $D = 485$ MHz [48]). To first order, ZFS does not alter the spin $-1/2 \rightarrow 1/2$ transition, but to second order, $E_{ZFS}^{(2)}(-\frac{1}{2} \rightarrow \frac{1}{2}) \propto \frac{D^2}{B_0}$, where B_0 is the strength of the applied magnetic field [35,49,50]. Therefore, in a typical field-swept EPR spectrum, only the narrow central transition is observed: the others are spread into a very broad background as a result of this strain at high field. Further, it has been shown that 240 GHz is close to the optimal frequency for Gd-sTPATCN, as it produces nearly the narrowest linewidth of all accessible EPR frequencies; this is a result of the competing effects of narrowing due to ZFS and increased broadening due to unresolved *g*-anisotropy [24].

3.2. Spectrometer sensitivity

For a 1 mM solution of Gd-sTPATCN spin label in D_2O, the SNR for 250 scans — using a conservative low-pass filter cutoff of 25 MHz — was found to be $\overline{SNR} = 60\pm10$ over 1000 experimental runs (see S.I. sec. S3.1 for walkthrough of SNR calculation). Because the SNR of rapid-scan is dependent on modulation coil frequency, number of averages, as well as digitizer and low-pass filter bandwidths, we sought to quantify our rapid-scan sensitivity by comparing it to the more well-established CW mode calculation. For CW, following the calculation in Nir-Arad et al. [51], the sensitivity, E, is:

$$E_{CW} = \frac{N}{SNR * n * \Delta H_{pp} * \sqrt{\Delta f}}, \tag{7}$$

where N is the number of spins in the sample (for 1.3 µL capillary of 1 mM Gd-sTPATCN, this is 7.8×10^{14} spins), SNR is the signal-to-noise ratio (8×10^3 in CW, see S.I. section S3.2), n is the number of EPR lines (1), ΔH_{pp} is the peak-to-peak linewidth (5 G), and Δf is the detection bandwidth (for a lock-in time constant of $\tau = 100$ ms with a 24 dB/oct roll-off, the equivalent noise bandwidth is $\Delta f = 5/64\tau = 0.78$ Hz [52]). Therefore, E_{CW} is:

$$E_{CW} = \frac{7.8 \times 10^{14} \text{ spins}}{8 \times 10^3 * 1 * 5 \text{ G} * \sqrt{0.78 \text{ Hz}}} = 2.2 \times 10^{10} \text{ spins/G} \sqrt{\text{Hz}}, \tag{8}$$

which is comparable to the room temperature, continuous wave sensitivities of other high-field, resonator-free spectrometers [21,51,53]. To compare rapid-scan to CW, it is simplest to divide the SNR of CW and rapid-scan by the square roots of their acquisition times, similar to what was done in Mitchell et al. [54]. In both cases, the SNR was carefully maximized by reducing high frequency noise as much as possible without distorting the line: for CW, this meant acquiring a point every 200 ms, twice the lock-in time constant; for rapid-scan, this meant using 2.5 MHz as the cut-off frequency for the digital low-pass filter, as any lower began to distort the lineshape (see S.I. Fig. S4). The SNR of CW was 8×10^3 and was acquired by sweeping over 11 mT with a 0.1 mT/s sweep rate, meaning the experiment took $t_{CW}^{acq} = 110$ s. The SNR of 2.5×10^4 averaged rapid-scan sweeps filtered at 2.5 MHz had a mean $\overline{SNR} = 1.7 \pm 0.6 \times 10^3$ over 9 experimental runs, acquired at 23.6 kHz, each with a total acquisition time, $t_{RS}^{acq} = 1.06$ s. Therefore,

$$SNR_{CW}/\sqrt{t_{CW}^{acq}} = 760 \sqrt{\text{Hz}}, \tag{9}$$

$$SNR_{RS}/\sqrt{t_{RS}^{acq}} = 1650 \sqrt{\text{Hz}}, \tag{10}$$

implying that while using UCSB's homebuilt EPR spectrometer, rapid-scan with a digital filter of 2.5 MHz can provide better SNR (and therefore sensitivity) in similar acquisition time. This approximately 2× improvement may be due to the elimination of phase noise between the source and the receiver as a result of the magnitude averaging scheme used. As discussed by Mitchell and collaborators [3,14,54], if the sample can be saturated with continuous wave excitation, even
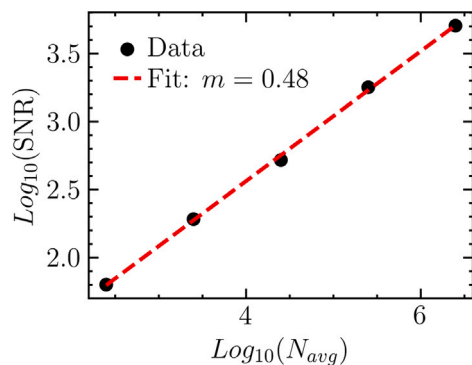
Fig. 3. Log–log plot of signal-to-noise (black dots) as a function of the number of rapid-scan acquisitions (*i.e.*, acquisition time). Up to at least 2.5×10^6 scans, the relationship is linear and the slope is $m = 0.48 \pm 0.2$ (fit shown by a dashed red line, uncertainty represents a 95% confidence interval for the fit), meaning SNR improves as expected, scaling as $\sqrt{N_{avg}}$. Sample was 1 mM Gd-sTPATCN in D_2O, experiment was done at 10 °C. Time and field-domain plots for each SNR are shown in S.I. Fig. S2.

larger SNR benefits may be obtained by using rapid-scan. In rapid-scan mode, higher source power may be used without saturating, which provides a much larger signal and thus higher SNR. However, Gd-sTPATCN at high field and room temperature cannot be saturated with the approximately 0.1 G B_1 field strength that is available at the sample position.

Rapid-scan also allows signal averaging for as long as is necessary, which is a marked improvement over CW at high field, where repeated signal averaging is difficult and source phase drift often negates its benefits. As shown in Fig. 3, longer acquisition times (more averages) improves SNR by the expected value of $\sqrt{N_{avg}}$, where N_{avg} is the number of summed signals. There are likely to be diminishing returns at some N_{avg}, when the amplitude of high frequency noise has been reduced below the resolution of the digitizer, but up to at least 2.5×10^6 scans (100 s), that limit had not been reached.

We can use Eq. (10) to estimate the SNR at the lower limit on time resolution (where each time step is a single low-to-high field sweep) for a 1 mM Gd-sTPATCN sample. Assuming a 23.6 kHz modulation frequency:

$$\text{SNR}_{RS} = 1650 \sqrt{\text{Hz}} * \sqrt{(23.6\,\text{kHz})^{-1}} = 10.7, \tag{11}$$

which would still be sufficient for the post-processing and linewidth fitting that is presented in Section 3.4 of this manuscript.

3.3. Continuous wave TiGGER of Gd-sTPATCN labeled AsLOV2

AsLOV2 is a phototropin 1 LOV2 domain (activated by light, oxygen, or voltage) that is found in *Avena sativa* (oats). It has a helix that is known to lose structure and unfold upon light activation [44,55,56]. We have previously demonstrated that AsLOV2, when doubly-labeled with Gd-sTPATCN at residues 406 and 537, exhibits spectroscopic dipolar broadening at high magnetic field [46]. This dipolar broadening was used to detect changes in inter-residue distance during and after protein activation with 450 nm light (see Fig. 4).

This dipolar broadening comes from a dipolar coupling term in the electron spin Hamiltonian and scales as $1/r^3$, where r is the distance between two nearby spin labels [50]:

$$\omega_{dd} = \frac{\mu_0}{4\pi} \frac{g^2 \mu_B^2}{\hbar r^3} (3\cos^2\theta - 1). \tag{12}$$

Here, ω_{dd} is the dipolar coupling strength in angular frequency units, μ_0 is the permeability of free space, g is the g-factor of the spin label ($g_{\text{Gd(III)}} \approx 1.99$ [57,58]), μ_B is the Bohr magneton, $\hbar$ is the reduced Planck constant, and θ is the polar angle between a vector connecting the two spins and the applied static magnetic field. Because nearly

100% of AsLOV2 proteins are doubly-labeled [46] and they are in a relatively dilute solution (1 mM), the dominant contribution to dipolar broadening is from the spins at the labeled sites [35]. Throughout this article, the chosen sites are the same as were reported in Maity et al. — 406 and 537 — which are known to be ~2.5 nm apart when immobilized [46,59]. The spin labels attached to these sites are slightly further apart (2.9 nm, estimated using off-rotamer sampling with chiLife [60,61]) than the sites themselves due to their rigid linkers. Upon 450 nm light activation, the Jα-helix unfolds, which allows site 537 to move further away from site 406 and thus reduces the dipolar coupling from $\omega_{dd}(r = 2.9\,\text{nm})$ to $\omega_{dd}(r > 2.9\,\text{nm})$. Fig. 4, reproduced from [46], presents this effect as a function of time before, during, and after light activation. It was observed that once the laser is turned off, the protein relaxes and refolds back to its dark state configuration with exponentially fitted relaxation time constant of $\tau = 51.9 \pm 0.3$ s.

3.4. Rapid-scan TiGGER of Gd-sTPATCN labeled AsLOV2

While the CW TiGGER spectra reported in Maity et al. [46] return information on the time scale and existence of inter-residue motion, time-dependent field-swept spectra are required for quantitative analysis of distances and distance distributions. A two-dimensional time-field map makes data interpretation more obvious and robust than one-dimensional information at a single field position, where artifacts can obscure a quantity of interest. For example, if light activation slightly changes the peak field position of a CW spectrum, the resulting one-dimensional transient would be indistinguishable from the peak signal decreasing due to linewidth broadening. With a RS field sweep, the quantity of interest can be extracted more reliably, as artifacts such as small field-dependent peak shifts can be handled in post-processing.

RS EPR is able resolve the entire Gd-sTPATCN central transition and continuously average as few as 250 scans per frame (totaling 10 ms), making it well-suited for the task of tracking AsLOV2's inter-residue movement. The shortest time resolution for continuous averaging is currently 10 ms due to a bottleneck of data transfer throughput and limited memory onboard the digitizer. However, the AsLOV2 spectra shown in Fig. 5a were averaged 25,000 times to achieve roughly 1 frame per second, which is sufficient for the timescale of the kinetics of interest (in our measurements, this timescale is ~100 s) while maximizing the signal-to-noise ratio and minimizing the amount of data that needs to be handled in post-processing. All RS TiGGER experiments presented here were captured in a single photocycle because averaging over multiple photocycles was not required to achieve a sufficient signal-to-noise ratio. As a result, the experiments presented here yield much more information than those in Maity et al. [46] while requiring only 10% of the acquisition time.

The AsLOV2 experiments presented in this manuscript were done in the presence of excess flavin mononucleotides (FMN), a chromophore that appears naturally in the protein's central binding pocket. FMN is responsible for absorbing a 450 nm photon and initiating AsLOV2's light-activated conformational changes. Preliminary results showed a correlation between dark-state linewidth and temperature that implied the protein seemed to "condense" with increasing temperature. However, loading excess FMN (100× the protein concentration) eliminated this effect: we suspect that the central FMN exchanged more readily between the center of the protein and the surrounding environment when it had more thermal energy. In the case of the FMN-surplus samples, the high concentration of external FMN ensured that an equilibrium was established with a higher fraction of loaded proteins. Therefore, to avoid a reduction in TiGGER sensitivity due to proteins lacking an FMN chromophore, all reported AsLOV2 RS TiGGER experiments were done with excess FMN at approximately 100 mM. All other spin labeling, purification, enrichment, and sample buffer details match what were reported in Maity et al. [46].
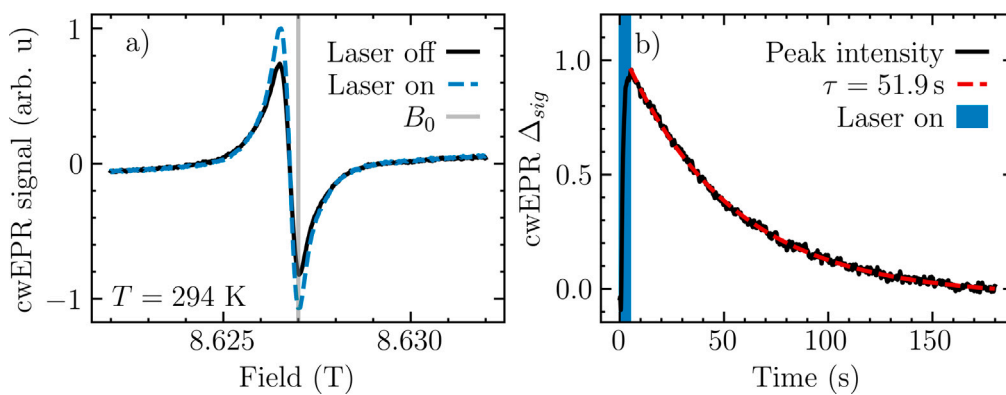
Fig. 4. 450 nm illumination inducing dipolar narrowing in AsLOV2 that was doubly labeled at residues 406 and 537. (a) Field-swept CW EPR demonstrates that the lineshape of light-activated, unfolded AsLOV2 (dashed blue) is narrower than the dark-state, folded AsLOV2 (solid black). Continuous wave EPR makes use of field modulation, resulting in the derivative lineshape shown; in this case, narrowing manifests as an increase in derivative peak height. (b) Time-dependent peak signal intensity as a result of unfolding (narrowing) and refolding (broadening) during and after light activation (vertical blue bar) at a fixed field position (gray vertical bar in a). The lineshape's peak height (black dots) showed a large narrowing during the laser illumination, and broadening during the relaxation afterward. An overlaid best fit (dashed red line) to an exponential decay provided a time constant of $\tau = 51.9 \pm 0.3$ s. ~1 mM liquid samples were loaded into a 100 μm-thick, 2-by-5 mm (approx. 1 μL sample volume) borosilicate glass capillary (VitroCom, USA) to maximize the sample surface area while minimizing THz absorption due to water [62]. Capillaries were wax-sealed, then placed on a PTFE tape covered, 7 mm diameter, protected silver planar mirror; no resonator was used. Experiment was done at 21 °C. Figures reproduced with permission from Maity et al. [46]. Copyright Wiley-VCH GmbH.
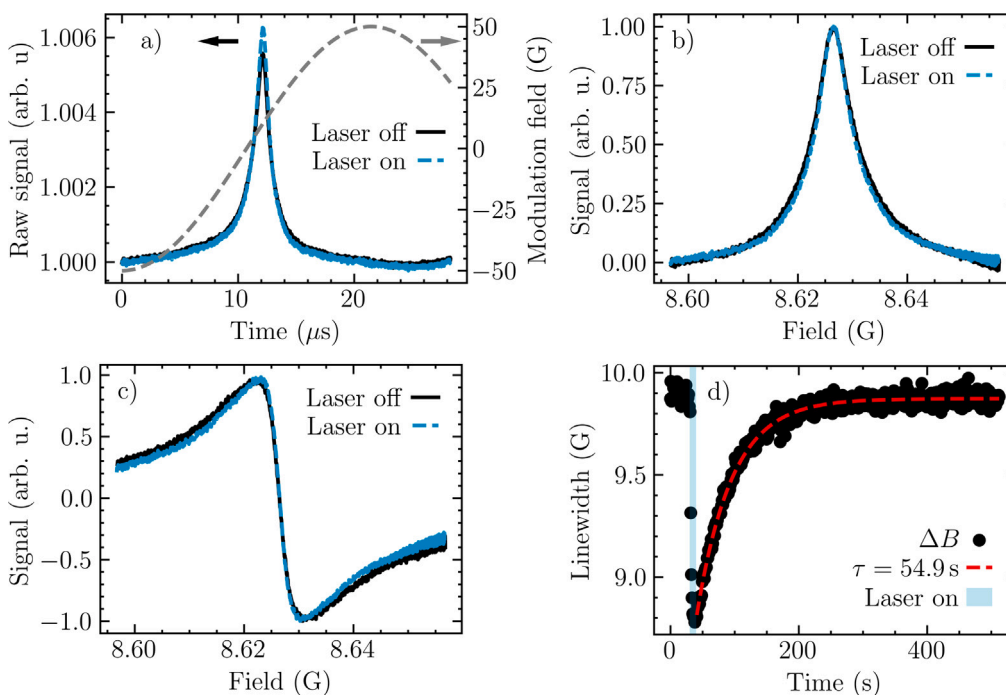

Fig. 5. Rapid-scan TiGGER of AsLOV2 doubly labeled with Gd-sTPATCN. (a) Raw rapid-scan data of 2.5×10^4 averages (black, at $t = 0$ s with the laser off, and dashed blue at $t = 40$ s, after the laser has been on for 10 s) and modulation field during the rapid-scan sweeps (dashed gray). Colored arrows point toward each line's respective *y*-axis. (b) Deconvolved rapid-scan absorptive data as a function of field and light activation (a video animation of this plot can be found in the Supplementary Material). Though only 2 frames are shown, roughly 500 were captured during the 500 s experimental run. When the protein was illuminated with 450 nm light, the linewidth narrowed, and then subsequently relaxed back toward the initial spectrum. The lineshapes are normalized to their individual peak intensities to highlight the light-induced narrowing. (c) Corresponding deconvolved rapid-scan dispersive data as a function of field and light activation. (d) Linewidth of doubly labeled AsLOV2 absorptive spectra as a function of time. Linewidths (black points) were extracted from Lorentzian fits of each rapid-scan frame captured during a TiGGER experiment. Fit of an exponential decay (dashed red) returned 54.9 ± 1.4 s, where the uncertainty represents a 95% confidence interval for the time constant returned by the fit. Samples were doubly labeled AsLOV2 at ~1 mM in buffer; the buffer included 100 mM surplus FMN. The experiment shown was done at 18 °C. Samples were loaded into a 100 μm-thick, 2-by-5 mm (approx. 1 μL sample volume) borosilicate glass capillary (VitroCom, Mountain Lakes, NJ) to maximize the ratio between surface area and sample thickness and thereby reduce 240 GHz attenuation [62].

To recover the refolding rate, the lineshape of each time-dependent RS TiGGER frame can be fitted to a Lorentzian,

$$\mathcal{L}(B) = \frac{A}{\pi} \frac{\frac{1}{2}\Delta B}{(B - B_0)^2 + (\frac{1}{2}\Delta B)^2}, \tag{13}$$

where A is the fit amplitude, B is the magnetic field, B_0 is the resonance position, and ΔB is the full-width at half-maximum in units of field. The

result of these fits for data recorded at 18 °C are shown in Fig. 5d. The 18 °C relaxation time (54.9 ± 1.4 s) agreed well with the CW experiment done at 21 °C (51.9 ± 0.3 s) in Maity et al. [46].

The experiment was repeated at a variety of temperatures from 6–33 °C (see S.I. Fig. S6). The relaxation times decrease with increasing temperature, as expected for a thermally-activated process per the Arrhenius equation, which states that the relaxation rate constant, k,
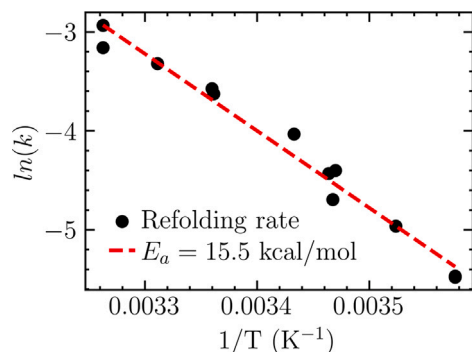
Fig. 6. Arrhenius plot of the natural logarithm of refolding rate (k; units of s^{-1}) of doubly labeled AsLOV2 versus inverse temperature. A linear fit (dashed red line) to the raw data (solid black dots) returned an activation energy $E_A = 15.5 \pm 1.5$ kcal/mol.

should behave according to

$$k = A\exp(-E_A/RT), \qquad (14)$$

where A is a scaling factor, E_A is the activation energy for a conformation change, R is the ideal gas constant, and T is temperature [63,64]. Rearranging,

$$ln(k) = ln(\tau^{-1}) = -\frac{E_A}{R}\frac{1}{T} + ln(A), \qquad (15)$$

which can be used to fit the natural log of the refolding rate to a linear equation in inverse temperature to extract an activation energy for refolding, E_A. The results of fitting the data to Eq. (15) are shown in Fig. 6. The extracted activation energy of 15.5 ± 1.5 kcal/mol is in good agreement with the value of 15.1 kcal/mol reported by Harper et al. [47], which was recorded using time-resolved NMR.

4. Discussion

We employed field-modulated rapid-scan TiGGER to record EPR lineshapes as a function of time during the photocycle of AsLOV2, which lasts hundreds of seconds, with a temporal resolution of approximately one second. The lineshape contains much more information than a similar CW TiGGER experiment, which samples the EPR spectrum at a fixed field as a function of time. The extra information yielded by RS includes entire lineshapes of Gd-sTPATCN's central transition that are robust to source phase and power drift. Such lineshapes are required to extract electronic dipolar couplings. Though current data throughput limits the time resolution to ~ 10 ms, corresponding to averaging ≥ 250 scans at 25 kHz, there is no fundamental reason that the temporal resolution cannot be decreased to well-below 1 ms, or even down to the time required for a single field-swept scan. As discussed above (see Eq. (11)), the SNR for a single scan would still be greater than 10. The data throughput can, in principle, be increased with improved digital hardware and software to enable time resolution into this single-scan regime. Further, the time required for a single-scan may be reduced by increasing the modulation frequency (potentially up to 1 MHz). With these hardware changes together with modest improvements in signal-to-noise ratio, for example by implementing a resonator, RS TiGGER should be able to resolve much faster dynamics (*e.g.*, the unfolding of AsLOV2, which has been reported to occur on 10–100 μs time scales [65]). To estimate the SNR at 1 MHz, we can use Eq. (10) while incorporating the effect of a resonator:

$$SNR(t^{acq} = 1\,\mu s) = 1650\ \sqrt{Hz}\sqrt{1\,\mu s} * \eta Q = 1.65 * \eta Q, \qquad (16)$$

where η is the filling factor and Q is the quality factor of the resonator [66,67]. For a high field-and-frequency system, a practical resonator candidate would be Fabry-Pérot [68,69] or open Fabry-Pérot [70–72] type, with Q-factors reported up to 10,000. However,

such high-Q EPR resonators have only been demonstrated at 94 GHz. More attainable Q-factors at 240 GHz, due to the smaller wavelengths (1.25 mm), is $Q \sim 100$, as reported in [73–76] in an open Fabry-Pérot configuration. To estimate η, which depends on resonator and sample relative sizes, we can use $\eta = 0.05$ from Burghaus et al. [77]. Therefore, ηQ would improve SNR by approximately 5, up to SNR ≈ 8, which is mainly limited by a low filling factor. Photonic bandgap resonators, by comparison, can achieve higher filling factors with comparable Q-factors at high frequency, with reported $Q \approx 450$ at 94 GHz [78]. Since the resonator structure can be scaled to smaller wavelengths quite easily, by simply reducing the thickness of dielectric layers, similar Qs should be achievable at 240 GHz. Conservatively assuming a photonic bandgap resonator has double the filling factor of Fabry-Pérot type ($\eta \approx 0.1$), a 240 GHz photonic bandgap resonator with $Q \approx 450$ would still increase the 1 μs SNR by a factor of 45, up to SNR ≈ 72.

The field-swept lineshapes recorded by RS TiGGER contain, in principle, all of the information required to extract inter-spin-label distance distributions as a function of time, rather than only qualitative changes as a result of deviation from the initial coupling strength. Quantitative distance distributions, obtained by fitting entire EPR lineshapes, can report on the entire ensemble of conformations rather than the mean of the population, which is especially important for intrinsically disordered regions of proteins. Further, using RS TiGGER to extract distance distributions *and* activation energies of kinetic processes simultaneously may allow for spectroscopic identification of conformational intermediates in multi-step unfolding or refolding processes, for example. For guidance on how extract distance distributions from EPR spectra, one can look to the extensive literature on the topic between nitroxide and gadolinium-based spin labels, including CW dipolar broadening [22,35,79–83], DEER and other pulsed techniques [50,84–88], and even R^{-6} dipolar relaxation effects in rapidly tumbling liquids [89,90].

Although addressing the challenges of extracting distance distributions from RS TiGGER lineshapes is beyond the scope of this paper, we briefly state two of them here, along with approaches to solving them. First, protein tumbling in solution reduces the dipolar broadening via motional narrowing [91,92]. Therefore, it is necessary to either (a) mitigate tumbling by slowing it down, for example using a viscogen like ficoll [93] or trehalose [94] which may not inhibit protein conformational changes, or (b) devise a method to quantify the incomplete motional averaging, possibly by direct spectral simulation of an intermediate motional regime using a tool such as EasySpin [95,96] with a rotational correlation time deduced from NMR [97,98] that is augmented by molecular dynamics simulation [99]. Second, while the distribution of zero-field splittings for Gd-sTPATCN has been measured at cryogenic temperatures [48], it may be different at room temperature, so further experimental or theoretical estimates are needed.

The payoff for successfully addressing these challenges is significant, as no other experimental methods we are aware of have the potential to measure time-resolved inter-residue distance distributions of proteins after photoactivation in solution state. DEER [100], cryo-electron microscopy [101], and X-ray crystallography [102,103] all provide high-resolution residue-residue distances, but they cannot be done in solution state. Förster resonance energy transfer (FRET) can be performed at room temperature, in solution, and even on single molecules. [104,105]. However, it is difficult to use FRET to extract more than a mean distance [106,107]. Combining FRET with freeze-quenching followed by DEER [108] or cryo-EM [109,110] will be helpful for benchmarking and validating approaches to extracting distance distributions from RS TiGGER.

5. Conclusion

In this article, we have demonstrated hardware and software upgrades to an existing CW EPR spectrometer that enable high-field rapid-scan EPR. RS preserves the central transition's entire time-dependent

lineshape as well as all of its underlying information, and can record an entire EPR spectrum in tens of microseconds, making it valuable for observing time-dependent kinetics that manifest as changes in the spectra. The SNR provided by our RS is approximately twice that of our CW EPR, after normalizing by the square root of acquisition time. The current lower limit on temporal resolution is approximately 10 ms, corresponding to 250 scans, which returned an average $\overline{SNR} = 60 \pm 10$ (when low-pass filtered at 25 MHz) for a 1 mM solution of Gd-sTPATCN labels in D_2O. Additionally, using the magnitude-averaging technique discussed, RS EPR enables averaging for long times (above 2.5×10^6 scans) while eliminating the typical susceptibility to source-receiver phase drift. The applicability of time-resolved, high-field RS EPR to the study of time-resolved protein conformational changes was demonstrated by "filming" the EPR spectrum as a function of time during a single photocycle, without the need for averaging over multiple experimental runs. In the future, the field-swept lineshape may be used to determine time-dependent distance distributions between spin labels in solution state. Further, time-resolved, high-field RS EPR may prove useful for "filming" other kinetic processes, potentially using different samples or spin labels, that can be observed through time-dependent lineshape changes of narrow-linewidth spectra.

CRediT authorship contribution statement

Brad D. Price: Conceptualization, Data curation, Formal analysis, Investigation, Methodology, Software, Visualization, Writing – original draft, Writing – review & editing. **Antonín Sojka:** Investigation, Methodology, Writing – original draft, Writing – review & editing. **Shiny Maity:** Resources, Writing – review & editing. **I. Marcelo Chavez:** Resources. **Matthieu Starck:** Resources. **Maxwell Z. Wilson:** Conceptualization, Funding acquisition, Investigation, Supervision. **Songi Han:** Conceptualization, Funding acquisition, Investigation, Project administration, Supervision, Writing – review & editing. **Mark S. Sherwin:** Conceptualization, Funding acquisition, Investigation, Project administration, Supervision, Writing – original draft, Writing – review & editing.

Declaration of competing interest

The authors declare that they have no known competing financial interests or personal relationships that could have appeared to influence the work reported in this paper.

Data availability

The data for the experiments presented here are hosted on Zenodo and available at https://doi.org/10.5281/zenodo.11062615.

Acknowledgments

Appendix A. Supplementary data

The Supplementary Material contains a Supplementary Information PDF with information regarding software and data processing as well as plots of multiple experimental runs that did not fit within the main text. The PDF includes links to all of the raw data presented in this manuscript, as well as the LabVIEW and Python3 code used to acquire and process it. The Supplementary Material also contains a "film" of the RS TiGGER lineshape of Gd-sTPATCN-labeled AsLOV2 during its photocycle.

Supplementary material related to this article can be found online at https://doi.org/10.1016/j.jmr.2024.107744.

References

[1] J.P. Joshi, J.R. Ballard, G.A. Rinard, R.W. Quine, S.S. Eaton, G.R. Eaton, Rapid-scan EPR with triangular scans and fourier deconvolution to recover the slow-scan spectrum, J. Magn. Reson. 175 (1) (2005) 44–51, http://dx.doi.org/10.1016/j.jmr.2005.03.013.

[2] M. Tseitlin, R.W. Quine, G.A. Rinard, S.S. Eaton, G.R. Eaton, Combining absorption and dispersion signals to improve signal-to-noise for rapid-scan EPR imaging, J. Magn. Reson. 203 (2) (2010) 305–310, http://dx.doi.org/10.1016/j.jmr.2010.01.013.

[3] D.G. Mitchell, R.W. Quine, M. Tseitlin, V. Meyer, S.S. Eaton, G.R. Eaton, Comparison of continuous wave, spin echo, and rapid scan EPR of irradiated fused quartz, Radiat. Meas. 46 (9) (2011) 993–996, http://dx.doi.org/10.1016/j.radmeas.2011.03.035.

[4] S.S. Eaton, R.W. Quine, M. Tseitlin, D.G. Mitchell, G.A. Rinard, G.R. Eaton, Rapid-Scan Electron Paramagnetic Resonance, Multifrequency Electron Paramagnetic Resonance: Data and Techniques, Wiley Online Library, 2014, pp. 3–67.

[5] S.S. Eaton, Y. Shi, L. Woodcock, L.A. Buchanan, J. McPeak, R.W. Quine, G.A. Rinard, B. Epel, H.J. Halpern, G.R. Eaton, Rapid-scan EPR imaging, J. Magn. Reson. 280 (2017) 140–148, http://dx.doi.org/10.1016/j.jmr.2017.02.013.

[6] O. Tseytlin, P. Guggilapu, A.A. Bobko, H. AlAhmad, X. Xu, B. Epel, R. O'Connell, E.H. Hoblitzell, T.D. Eubank, V.V. Khramtsov, B. Driesschaert, E. Kazkaz, M. Tseytlin, Modular imaging system: Rapid scan EPR at 800 MHz, J. Magn. Reson. 305 (2019) 94–103, http://dx.doi.org/10.1016/j.jmr.2019.06.003.

[7] D.J. McCrory, M.A. Anders, J.T. Ryan, P.R. Shrestha, K.P. Cheung, P.M. Lenahan, J.P. Campbell, Slow- and rapid-scan frequency-swept electrically detected magnetic resonance of MOSFETs with a non-resonant microwave probe within a semiconductor wafer-probing station, Rev. Sci. Instrum. 90 (1) (2019) 014708, http://dx.doi.org/10.1063/1.5053665.

[8] U. Eichhoff, P. Höfer, 75 years of EPR. EPR milestones in 60 years Bruker history, Appl. Magn. Reson. 51 (12) (2020) 1723–1737, http://dx.doi.org/10.1007/s00723-020-01221-1.

[9] M.A. Hassan, T. Elrifai, A. Sakr, M. Kern, K. Lips, J. Anders, A 14-channel 7 GHz VCO-based EPR-on-a-chip sensor with rapid scan capabilities, in: 2021 IEEE Sensors, 2021, pp. 1–4, http://dx.doi.org/10.1109/SENSORS47087.2021.9639513.

[10] S. Künstner, A. Chu, K.-P. Dinse, A. Schnegg, J.E. McPeak, B. Naydenov, J. Anders, K. Lips, Rapid-scan electron paramagnetic resonance using an EPR-on-a-Chip sensor, Magn. Reson. 2 (2) (2021) 673–687, http://dx.doi.org/10.5194/mr-2-673-2021.

[11] G.R. Eaton, S.S. Eaton, Chapter one - advances in rapid scan EPR spectroscopy, in: R.D. Britt (Ed.), Methods in Enzymology, in: Advances in Biomolecular EPR, vol. 666, Academic Press, 2022, pp. 1–24, http://dx.doi.org/10.1016/bs.mie.2022.02.013.

[12] S.A. Jacobs, G.W. Kramer, R.E. Santini, D.W. Margerum, A rapid-scanning electron paramagnetic resonance spectrometer with stopped-flow mixing, Anal. Chim. Acta 157 (1984) 117–124, http://dx.doi.org/10.1016/S0003-2670(00)83611-9.

[13] A. Sienkiewicz, A.M.d.C. Ferreira, B. Danner, C.P. Scholes, Dielectric resonator-based flow and stopped-flow EPR with rapid field scanning: A methodology for increasing kinetic information, J. Magn. Reson. 136 (2) (1999) 137–142, http://dx.doi.org/10.1006/jmre.1998.1630.

[14] D.G. Mitchell, G.M. Rosen, M. Tseitlin, B. Symmes, S.S. Eaton, G.R. Eaton, Use of rapid-scan EPR to improve detection sensitivity for spin-trapped radicals, Biophys. J. 105 (2) (2013) 338–342, http://dx.doi.org/10.1016/j.bpj.2013.06.005.

[15] H. Elajaili, J.R. Biller, G.M. Rosen, J.P.Y. Kao, M. Tseytlin, L.A. Buchanan, G.A. Rinard, R.W. Quine, J. McPeak, Y. Shi, S.S. Eaton, G.R. Eaton, Imaging disulfide dinitroxides at 250 MHz to monitor thiol redox status, J. Magn. Reson. 260 (2015) 77–82, http://dx.doi.org/10.1016/j.jmr.2015.08.027.

[16] G.R. Eaton, S.S. Eaton, Rapid-scan electron paramagnetic resonance, in: EMagRes, John Wiley & Sons, Ltd, 2016, pp. 1529–1542, http://dx.doi.org/10.1002/9780470034590.emrstm1522.

[17] A. Sojka, B.D. Price, M.S. Sherwin, Order-of-magnitude SNR improvement for high-field EPR spectrometers via 3D printed quasi-optical sample holders, Sci. Adv. 9 (38) (2023) eadi7412, http://dx.doi.org/10.1126/sciadv.adi7412.

[18] O. Laguta, M. Tuček, J. van Slageren, P. Neugebauer, Multi-frequency rapid-scan HFEPR, J. Magn. Reson. 296 (2018) 138–142, http://dx.doi.org/10.1016/j.jmr.2018.09.005.

[19] K. Khan, M.A. Hassan, M. Kern, K. Lips, I. Schwartz, M. Plenio, F. Jelezko, J. Anders, A 12.2 to 14.9 GHz injection-locked VCO array with an on-chip 50 MHz BW semi-digital PLL for transient spin manipulation and detection, in: 2022 IEEE 65th International Midwest Symposium on Circuits and Systems, MWSCAS, 2022, pp. 1–4, http://dx.doi.org/10.1109/MWSCAS54063.2022.9859288, ISSN: 1558-3899.

[20] M. Tseitlin, G.A. Rinard, R.W. Quine, S.S. Eaton, G.R. Eaton, Rapid frequency scan EPR, J. Magn. Reson. 211 (2) (2011) 156–161, http://dx.doi.org/10.1016/j.jmr.2011.05.006.

[21] A. Sojka, Development of a Novel Terahertz Magnetic Resonance Spectrometer for Spin Dynamics Investigations (Ph.D. thesis), BRNO UNIVERSITY OF TECHNOLOGY, Brno, CZ, 2022, URL: https://theses.cz/id/hf5kw2/Dizertace_Sojka.pdf.

[22] J.A. Clayton, M. Qi, A. Godt, D. Goldfarb, S. Han, M.S. Sherwin, Gd^{3+}–Gd^{3+} distances exceeding 3 nm determined by very high frequency continuous wave electron paramagnetic resonance, Phys. Chem. Chem. Phys. 19 (7) (2017) 5127–5136, http://dx.doi.org/10.1039/C6CP07119H.

[23] A. Shah, A. Roux, M. Starck, J.A. Mosely, M. Stevens, D.G. Norman, R.I. Hunter, H. El Mkami, G.M. Smith, D. Parker, J.E. Lovett, A gadolinium spin label with both a narrow central transition and short tether for use in double electron electron resonance distance measurements, Inorg. Chem. 58 (5) (2019) 3015–3025, http://dx.doi.org/10.1021/acs.inorgchem.8b02892.

[24] T. Dubroca, X. Wang, F. Mentink-Vigier, B. Trociewitz, M. Starck, D. Parker, M.S. Sherwin, S. Hill, J. Krzystek, Terahertz EPR spectroscopy using a 36-tesla high-homogeneity series-connected hybrid magnet, J. Magn. Reson. 353 (2023) 107480, http://dx.doi.org/10.1016/j.jmr.2023.107480.

[25] J.S. Hyde, R.A. Strangeway, T.G. Camenisch, J.J. Ratke, W. Froncisz, W-band frequency-swept EPR, J. Magn. Reson. 205 (1) (2010) 93–101, http://dx.doi.org/10.1016/j.jmr.2010.04.005.

[26] O. Laguta, A. Sojka, A. Marko, P. Neugebauer, Rapid scan ESR: A versatile tool for the spin relaxation studies at (sub)THz frequencies, Appl. Phys. Lett. 120 (12) (2022) 120502, http://dx.doi.org/10.1063/5.0083010.

[27] W.R. Briggs, J.M. Christie, Phototropins 1 and 2: versatile plant blue-light receptors, Trends in Plant Science 7 (5) (2002) 204–210, http://dx.doi.org/10.1016/S1360-1385(02)02245-8.

[28] R.B. Celaya, E. Liscum, Phototropins and Associated Signaling: Providing the Power of Movement in Higher Plants, Photochemistry and Photobiology 81 (1) (2005) 73–80, http://dx.doi.org/10.1111/j.1751-1097.2005.tb01524.x.

[29] O. Dagliyan, M. Tarnawski, P.-H. Chu, D. Shirvanyants, I. Schlichting, N.V. Dokholyan, K.M. Hahn, Engineering extrinsic disorder to control protein activity in living cells, Science 354 (6318) (2016) 1441–1444, http://dx.doi.org/10.1126/science.aah3404.

[30] A. Losi, K.H. Gardner, A. Möglich, Blue-light receptors for optogenetics, Chem. Rev. 118 (21) (2018) 10659–10709, http://dx.doi.org/10.1021/acs.chemrev.8b00163.

[31] C. Carrasco-López, E.M. Zhao, A.A. Gil, N. Alam, J.E. Toettcher, J.L. Avalos, Development of light-responsive protein binding in the monobody nonimmunoglobulin scaffold, Nature Commun. 11 (1) (2020) 4045, http://dx.doi.org/10.1038/s41467-020-17837-7.

[32] A.A. Gil, C. Carrasco-López, L. Zhu, E.M. Zhao, P.T. Ravindran, M.Z. Wilson, A.G. Goglia, J.L. Avalos, J.E. Toettcher, Optogenetic control of protein binding using light-switchable nanobodies, Nature Commun. 11 (1) (2020) 4044, http://dx.doi.org/10.1038/s41467-020-17836-8.

[33] K.Y. Manoilov, V.V. Verkhusha, D.M. Shcherbakova, A guide to the optogenetic regulation of endogenous molecules, Nat. Methods 18 (9) (2021) 1027–1037, http://dx.doi.org/10.1038/s41592-021-01240-1.

[34] S. Takahashi, L.-C. Brunel, D.T. Edwards, J. van Tol, G. Ramian, S. Han, M.S. Sherwin, Pulsed electron paramagnetic resonance spectroscopy powered by a free-electron laser, Nature 489 (7416) (2012) 409–413, http://dx.doi.org/10.1038/nature11437.

[35] D.T. Edwards, High-Field EPR for Studies of Structure in Biological Systems (Ph.D. thesis), University of California, Santa Barbara, Santa Barbara, CA, 2013, URL: https://sherwingroup.itst.ucsb.edu/wp-content/upload/theses/DevinEdwardsSep2013.pdf.

[36] F.E. Terman, Radio Engineers' Handbook, first ed., McGraw-Hill Book Co., Inc., New York, 1943.

[37] R.W. Quine, T. Czechowski, G.R. Eaton, A linear magnetic field scan driver, Concepts Magn. Reson. B 35B (1) (2009) 44–58, http://dx.doi.org/10.1002/cmr.b.20128.

[38] I. Kaminker, A. Potapov, A. Feintuch, S. Vega, D. Goldfarb, Population transfer for signal enhancement in pulsed EPR experiments on half integer high spin systems, Phys. Chem. Chem. Phys. 11 (31) (2009) 6799, http://dx.doi.org/10.1039/b906177k.

[39] A.W. Kittell, T.G. Camenisch, J.J. Ratke, J.W. Sidabras, J.S. Hyde, Detection of undistorted continuous wave (CW) electron paramagnetic resonance (EPR) spectra with non-adiabatic rapid sweep (NARS) of the magnetic field, J. Magn. Reson. 211 (2) (2011) 228–233, http://dx.doi.org/10.1016/j.jmr.2011.06.004.

[40] R.W. Quine, D.G. Mitchell, M. Tseitlin, S.S. Eaton, G.R. Eaton, A resonated coil driver for rapid scan EPR, Concepts Magn. Reson. B 41B (4) (2012) 95–110, http://dx.doi.org/10.1002/cmr.b.21222.

[41] M. Tseytlin, General solution for rapid scan EPR deconvolution problem, J. Magn. Reson. 318 (2020) 106801, http://dx.doi.org/10.1016/j.jmr.2020.106801.

[42] B.D. Price, brad-ley/rapidscan-epr: 2023-10-24, 2023, http://dx.doi.org/10.5281/zenodo.10038328.

[43] scipy.signal.hilbert — SciPy v1.12.0 Manual, 2024, URL: https://docs.scipy.org/doc/scipy/reference/generated/scipy.signal.hilbert.html.

[44] S.M. Harper, L.C. Neil, K.H. Gardner, Structural basis of a phototropin light switch, Science 301 (5639) (2003) 1541–1544, http://dx.doi.org/10.1126/science.1086810.

[45] A. Feintuch, G. Otting, D. Goldfarb, Gd3+ spin labeling for measuring distances in biomacromolecules: why and how? in: Methods in Enzymology, Vol. 563, Elsevier, 2015, pp. 415–457.

[46] S. Maity, B.D. Price, C.B. Wilson, A. Mukherjee, M. Starck, D. Parker, M.Z. Wilson, J.E. Lovett, S. Han, M.S. Sherwin, Triggered functional dynamics of AsLOV2 by time-resolved electron paramagnetic resonance at high magnetic fields, Angew. Chem. Int. Ed. 62 (13) (2023) e202212832, http://dx.doi.org/10.1002/anie.202212832.

[47] S.M. Harper, I.J. Day, P.J. Hore, K.H. Gardner, Conformational changes in a photosensory LOV domain monitored by time-resolved NMR spectroscopy, J. Am. Chem. Soc. 126 (11) (2004) 3390–3391, http://dx.doi.org/10.1021/ja038224f.

[48] J. A. Clayton, K. Keller, M. Qi, J. Wegner, V. Koch, H. Hintz, A. Godt, S. Han, G. Jeschke, M. S. Sherwin, M. Yulikov, Quantitative analysis of zero-field splitting parameter distributions in Gd(III) complexes, Phys. Chem. Chem. Phys. 20 (15) (2018) 10470–10492, http://dx.doi.org/10.1039/C7CP08507A.

[49] E. Meirovitch, R. Poupko, Line shape studies of the electron spin resonance spectra of manganese protein complexes, J. Phys. Chem. 82 (17) (1978) 1920–1925, http://dx.doi.org/10.1021/j100506a013.

[50] D. Goldfarb, Gd3+ spin labeling for distance measurements by pulse EPR spectroscopy, Phys. Chem. Chem. Phys. 16 (21) (2014) 9685–9699, http://dx.doi.org/10.1039/C3CP53822B.

[51] O. Nir-Arad, D.H. Shlomi, A. Israelstam, T. Amit, N. Manukovsky, A.B. Fialkov, I. Kaminker, The CW-EPR capabilities of a dual DNP/EPR spectrometer operating at 14 and 7 T, J. Magn. Reson. 360 (2024) 107635, http://dx.doi.org/10.1016/j.jmr.2024.107635.

[52] S.R. Systems, Model SR830 - DSP lock-in amplifier, 2011, URL: https://www.thinksrs.com/products/sr830.html.

[53] P. Neugebauer, D. Bloos, R. Marx, P. Lutz, M. Kern, D. Aguilà, J. Vaverka, O. Laguta, C. Dietrich, R. Clérac, J.v. Slageren, Ultra-broadband EPR spectroscopy in field and frequency domains, Phys. Chem. Chem. Phys. 20 (22) (2018) 15528–15534, http://dx.doi.org/10.1039/C7CP07443C.

[54] D.G. Mitchell, M. Tseitlin, R.W. Quine, V. Meyer, M.E. Newton, A. Schnegg, B. George, S.S. Eaton, G.R. Eaton, X-band rapid-scan EPR of samples with long electron spin relaxation times: a comparison of continuous wave, pulse and rapid-scan EPR, Mol. Phys. 111 (18–19) (2013) 2664–2673, http://dx.doi.org/10.1080/00268976.2013.792959.

[55] T.E. Swartz, S.B. Corchnoy, J.M. Christie, J.W. Lewis, I. Szundi, W.R. Briggs, R.A. Bogomolni, The photocycle of a flavin-binding domain of the blue light photoreceptor phototropin, J. Biol. Chem. 276 (39) (2001) 36493–36500, http://dx.doi.org/10.1074/jbc.M103114200.

[56] T.E. Swartz, P.J. Wenzel, S.B. Corchnoy, W.R. Briggs, R.A. Bogomolni, Vibration spectroscopy reveals light-induced chromophore and protein structural changes in the LOV2 domain of the plant blue-light receptor phototropin 1, Biochemistry 41 (23) (2002) 7183–7189, http://dx.doi.org/10.1021/bi025861u.

[57] T.I. Smirnova, A.I. Smirnov, R.L. Belford, R.B. Clarkson, Interaction of Gd(III) MRI contrast agents with membranes: a review of recent EPR studies, Magn. Reson. Mater. Phys. Biol. Med. 8 (3) (1999) 214–229, http://dx.doi.org/10.1007/BF02594601.

[58] R.W. Reynolds, L.A. Boatner, C.B. Finch, A. Chatelain, M.M. Abraham, EPR investigations of Er3+, Yb3+, and Gd3+ in zircon-structure silicates, J. Chem. Phys. 56 (11) (2003) 5607–5625, http://dx.doi.org/10.1063/1.1677080.

[59] A.S. Halavaty, K. Moffat, N- and C-terminal flanking regions modulate light-induced signal transduction in the LOV2 domain of the blue light sensor phototropin 1 from avena sativa, Biochemistry 46 (49) (2007) 14001–14009, http://dx.doi.org/10.1021/bi701543e.

[60] M.H. Tessmer, E.R. Canarie, S. Stoll, Comparative evaluation of spin-label modeling methods for protein structural studies, Biophys. J. 121 (18) (2022) 3508–3519, http://dx.doi.org/10.1016/j.bpj.2022.08.002.

[61] M.H. Tessmer, S. Stoll, chiLife: An open-source Python package for in silico spin labeling and integrative protein modeling, PLoS Comput. Biol. 19 (3) (2023) e1010834, http://dx.doi.org/10.1371/journal.pcbi.1010834.

[62] C.B. Wilson, Adventures in High-field Electron Paramagnetic Resonance - ProQuest (Ph.D. thesis), University of California, Santa Barbara, Santa Barbara, CA, 2019.

[63] S. Arrhenius, Über die dissociationswärme und den einfluss der temperatur auf den dissociationsgrad der elektrolyte, Z. Phys. Chem. 4U (1) (1889) 96–116, http://dx.doi.org/10.1515/zpch-1889-0408.

[64] K.J. Laidler, The development of the Arrhenius equation, J. Chem. Educ. 61 (6) (1984) 494, http://dx.doi.org/10.1021/ed061p494.

[65] J.N. Iuliano, J.T. Collado, A.A. Gil, P.T. Ravindran, A. Lukacs, S. Shin, H.A. Woroniecka, K. Adamczyk, J.M. Aramini, U.R. Edupuganti, C.R. Hall, G.M. Greetham, I.V. Sazanovich, I.P. Clark, T. Daryaee, J.E. Toettcher, J.B. French, K.H. Gardner, C.L. Simmerling, S.R. Meech, P.J. Tonge, Unraveling the mechanism of a LOV domain optogenetic sensor: A glutamine lever induces unfolding of the Jα Helix, ACS Chem. Biol. 15 (10) (2020) 2752–2765, http://dx.doi.org/10.1021/acschembio.0c00543.

[66] G.A. Rinard, R.W. Quine, R. Song, G.R. Eaton, S.S. Eaton, Absolute EPR spin echo and noise intensities, J. Magn. Reson. 140 (1) (1999) 69–83, http://dx.doi.org/10.1006/jmre.1999.1823.

[67] G.R. Eaton, S.S. Eaton, D.P. Barr, R.T. Weber, Quantitative EPR, Springer Science & Business Media, 2010, Google-Books-ID: sayWdlbWGfwC.

[68] E. Haindl, K. Möbius, A 94 GHz EPR spectrometer with Fabry–Perot resonator, Z. Nat.forsch. A 40 (2) (1985) 169–172, http://dx.doi.org/10.1515/zna-1985-0211.

[69] I. Tkach, U. Rogulis, S. Greulich-Weber, J.-M. Spaeth, W-band Fabry–Pérot microwave reasonators for optical detected electron paramagnetic resonance and electron nuclear double resonance of paramagnetic defects in solids, Rev. Sci. Instrum. 75 (11) (2004) 4781–4788, http://dx.doi.org/10.1063/1.1809291.

[70] I. Amity, A Fabry–Perot cavity for millimeter and submillimeter ESR spectrometers, Rev. Sci. Instrum. 41 (10) (1970) 1492–1494.

[71] R.T. Weber, J.A.J.M. Disselhorst, L.J. Prevo, J. Schmidt, W.T.H. Wenckebach, Electron spin-echo spectroscopy at 95 GHz, J. Magn. Reson. (1969) 81 (1) (1989) 129–144, http://dx.doi.org/10.1016/0022-2364(89)90272-2.

[72] G.M. Smith, J.C.G. Lesurf, R.H. Mitchell, P.C. Riedi, Quasi-optical cw mm-wave electron spin resonance spectrometer, Rev. Sci. Instrum. 69 (11) (1998) 3924–3937, http://dx.doi.org/10.1063/1.1149200.

[73] D.E. Budil, K.A. Earle, W.B. Lynch, J.H. Freed, Electron paramagnetic resonance at 1 millimeter wavelengths, in: Advanced EPR, Elsevier, 1989, pp. 307–340.

[74] K.A. Earle, D.E. Budil, J.H. Freed, 250-GHz EPR of nitroxides in the slow-motional regime: models of rotational diffusion, J. Phys. Chem. 97 (50) (1993) 13289–13297, http://dx.doi.org/10.1021/j100152a037.

[75] M. Rohrer, J. Krzystek, V. Williams, L.-C. Brunel, Fabry–Perot resonator for high-field multi-frequency ESR at millimetre and submillimetre wavelengths, Meas. Sci. Technol. 10 (4) (1999) 275, http://dx.doi.org/10.1088/0957-0233/10/4/003.

[76] M.R. Fuchs, T.F. Prisner, K. Möbius, A high-field/high-frequency heterodyne induction-mode electron paramagnetic resonance spectrometer operating at 360 GHz, Rev. Sci. Instrum. 70 (9) (1999) 3681–3683, http://dx.doi.org/10.1063/1.1149977.

[77] O. Burghaus, M. Rohrer, T. Gotzinger, M. Plato, K. Mobius, A novel high-field/high-frequency EPR and ENDOR spectrometer operating at 3 mm wavelength, Meas. Sci. Technol. 3 (8) (1992) 765, http://dx.doi.org/10.1088/0957-0233/3/8/013.

[78] S. Milikisiyants, A.A. Nevzorov, A.I. Smirnov, Photonic band-gap resonators for high-field/high-frequency EPR of microliter-volume liquid aqueous samples, J. Magn. Reson. 296 (2018) 152–164, http://dx.doi.org/10.1016/j.jmr.2018.09.006.

[79] W.B. Gleason, R.E. Barnett, Use of the point dipole approximation for nitroxide biradicals, J. Am. Chem. Soc. 98 (10) (1976) 2701–2705, http://dx.doi.org/10.1021/ja00426a003.

[80] M.D. Rabenstein, Y.K. Shin, Determination of the distance between two spin labels attached to a macromolecule, Proc. Natl. Acad. Sci. 92 (18) (1995) 8239–8243, http://dx.doi.org/10.1073/pnas.92.18.8239.

[81] T.E. Thorgeirsson, W. Xiao, L.S. Brown, R. Needleman, J.K. Lanyi, Y.-K. Shin, Transient channel-opening in bacteriorhodopsin: an EPR study, J. Mol. Biol. 273 (5) (1997) 951–957, http://dx.doi.org/10.1006/jmbi.1997.1362.

[82] W.L. Hubbell, D.S. Cafiso, C. Altenbach, Identifying conformational changes with site-directed spin labeling, Nat. Struct. Biol. 7 (9) (2000) 735–739, http://dx.doi.org/10.1038/78956.

[83] A. Czogalla, A. Pieciul, A. Jezierski, A. Sikorski, Attaching a spin to a protein-site-directed spin labeling in structural biology, Acta Biochim. Polon. 54 (2) (2007) 235–244.

[84] G. Jeschke, Distance measurements in the nanometer range by pulse EPR, ChemPhysChem 3 (11) (2002) 927–932, http://dx.doi.org/10.1002/1439-7641(20021115)3:11<927::AID-CPHC927>3.0.CO;2-Q.

[85] H.-J. Steinhoff, Inter- and intra-molecular distances determined by EPR spectroscopy and site-directed spin labeling reveal protein-protein and protein-oligonucleotide interaction, Biol. Chem., 385 (10) (2004) 913–920, http://dx.doi.org/10.1515/BC.2004.119.

[86] M. Pannier, S. Veit, A. Godt, G. Jeschke, H.W. Spiess, Dead-time free measurement of dipole–dipole interactions between electron spins, J. Magn. Reson. 213 (2) (2011) 316–325, http://dx.doi.org/10.1016/j.jmr.2011.08.035.

[87] A. Doll, M. Qi, N. Wili, S. Pribitzer, A. Godt, G. Jeschke, Gd(III)–Gd(III) distance measurements with chirp pump pulses, J. Magn. Reson. 259 (2015) 153–162, http://dx.doi.org/10.1016/j.jmr.2015.08.010.

[88] P.P. Borbat, A.J. Costa-Filho, K.A. Earle, J.K. Moscicki, J.H. Freed, Electron spin resonance in studies of membranes and proteins, Science 291 (5502) (2001) 266–269, http://dx.doi.org/10.1126/science.291.5502.266.

[89] H.S. Mchaourab, K.J. Oh, C.J. Fang, W.L. Hubbell, Conformation of T4 lysozyme in solution. hinge-bending motion and the substrate-induced conformational transition studied by site-directed spin labeling, Biochemistry 36 (2) (1997) 307–316, http://dx.doi.org/10.1021/bi962114m.

[90] J.A. Cooke, L.J. Brown, Distance measurements by continuous wave EPR spectroscopy to monitor protein folding, in: A.F. Hill, K.J. Barnham, S.P. Bottomley, R. Cappai (Eds.), Protein Folding, Misfolding, and Disease: Methods and Protocols, in: Methods in Molecular Biology, Humana Press, Totowa, NJ, 2011, pp. 73–96, http://dx.doi.org/10.1007/978-1-60327-223-0_6.

[91] P. W. Anderson, A mathematical model for the narrowing of spectral lines by exchange or motion, J. Phys. Soc. Japan 9 (3) (1954) 316–339, http://dx.doi.org/10.1143/JPSJ.9.316.

[92] J.-P. Korb, D.C. Torney, H.M. McConnell, Dipolar correlation function and motional narrowing in finite two-dimensional spin systems, J. Chem. Phys. 78 (9) (1983) 5782–5789, http://dx.doi.org/10.1063/1.445434.

[93] Z. Zhang, M.R. Fleissner, D.S. Tipikin, Z. Liang, J.K. Moscicki, K.A. Earle, W.L. Hubbell, J.H. Freed, Multifrequency electron spin resonance study of the dynamics of spin labeled T4 lysozyme, J. Phys. Chem. B 114 (16) (2010) 5503–5521, http://dx.doi.org/10.1021/jp910606h.

[94] C. Hackel, T. Zinkevich, P. Belton, A. Achilles, D. Reichert, A. Krushelnitsky, The trehalose coating effect on the internal protein dynamics, Phys. Chem. Chem. Phys. 14 (8) (2012) 2727–2734, http://dx.doi.org/10.1039/C2CP23098D.

[95] EasySpin, Simulating slow-motion cw EPR spectra, 2023.

[96] J. Lehner, S. Stoll, Modeling of motional EPR spectra using hindered Brownian rotational diffusion and the stochastic Liouville equation, J. Chem. Phys. 152 (9) (2020) 094103, http://dx.doi.org/10.1063/1.5139935.

[97] L.E. Kay, D.A. Torchia, A. Bax, Backbone dynamics of proteins as studied by nitrogen-15 inverse detected heteronuclear NMR spectroscopy: application to staphylococcal nuclease, Biochemistry 28 (23) (1989) 8972–8979, http://dx.doi.org/10.1021/bi00449a003.

[98] D. Lee, C. Hilty, G. Wider, K. Wüthrich, Effective rotational correlation times of proteins from NMR relaxation interference, J. Magn. Reson. 178 (1) (2006) 72–76, http://dx.doi.org/10.1016/j.jmr.2005.08.014.

[99] O.H.S. Ollila, H.A. Heikkinen, H. Iwaï, Rotational dynamics of proteins from spin relaxation times and molecular dynamics simulations, J. Phys. Chem. B 122 (25) (2018) 6559–6569, http://dx.doi.org/10.1021/acs.jpcb.8b02250.

[100] G. Jeschke, DEER distance measurements on proteins, Annu. Rev. Phys. Chem. 63 (Volume 63, 2012) (2012) 419–446, http://dx.doi.org/10.1146/annurev-physchem-032511-143716.

[101] X. Benjin, L. Ling, Developments, applications, and prospects of cryo-electron microscopy, Protein Sci. 29 (4) (2020) 872–882, http://dx.doi.org/10.1002/pro.3805.

[102] G.A. Petsko, D. Ringe, Fluctuations in protein structure from X-ray diffraction, Annu. Rev. Biophys. Bioeng. 13 (1) (1984) 331–371.

[103] A. Ilari, C. Savino, Protein structure determination by X-ray crystallography, in: J.M. Keith (Ed.), Bioinformatics: Data, Sequence Analysis and Evolution, Humana Press, Totowa, NJ, 2008, pp. 63–87, http://dx.doi.org/10.1007/978-1-60327-159-2_3.

[104] V. Helms, Principles of Computational Cell Biology: From Protein Complexes to Cellular Networks, John Wiley & Sons, 2008.

[105] R. Roy, S. Hohng, T. Ha, A practical guide to single-molecule FRET, Nat. Methods 5 (6) (2008) 507–516, http://dx.doi.org/10.1038/nmeth.1208.

[106] E. Lerner, T. Orevi, E. Ben Ishay, D. Amir, E. Haas, Kinetics of fast changing intramolecular distance distributions obtained by combined analysis of FRET efficiency kinetics and time-resolved FRET equilibrium measurements, Biophys. J. 106 (3) (2014) 667–676, http://dx.doi.org/10.1016/j.bpj.2013.11.4500.

[107] E.D. Holmstrom, A. Holla, W. Zheng, D. Nettels, R.B. Best, B. Schuler, Chapter ten - accurate transfer efficiencies, distance distributions, and ensembles of unfolded and intrinsically disordered proteins from single-molecule FRET, in: E. Rhoades (Ed.), Methods in Enzymology, in: Intrinsically Disordered Proteins, vol. 611, Academic Press, 2018, pp. 287–325, http://dx.doi.org/10.1016/bs.mie.2018.09.030.

[108] E.R. Georgieva, A.S. Roy, V.M. Grigoryants, P.P. Borbat, K.A. Earle, C.P. Scholes, J.H. Freed, Effect of freezing conditions on distances and their distributions derived from double electron electron resonance (DEER): A study of doubly-spin-labeled T4 lysozyme, J. Magn. Reson. 216 (2012) 69–77, http://dx.doi.org/10.1016/j.jmr.2012.01.004.

[109] D. Elmlund, S.N. Le, H. Elmlund, High-resolution cryo-EM: the nuts and bolts, Curr. Opin. Struct. Biol. 46 (2017) 1–6, http://dx.doi.org/10.1016/j.sbi.2017.03.003.

[110] S.J. Amann, D. Keihsler, T. Bodrug, N.G. Brown, D. Haselbach, Frozen in time: analyzing molecular dynamics with time-resolved cryo-EM, Structure 31 (1) (2023) 4–19.